Geologie en Mijnbouw **77:** 137–151, 1999.

Imaging spectrometry for geological remote sensing

Freek van der Meer
International Institute for Aerospace Surveys and Earth Sciences ITC, Division of Geological Survey, Hengelosestraat 99, 7534 AE Enschede, the Netherlands

Received 4 January 1997; accepted in revised form 17 December 1998

Key words: absorption-feature mapping, Cuprite mining district, high-spectral resolution, mineralogy, Nevada

Abstract

Without use of imaging spectrometry, imaging of the Earth's surface from aircraft and from spacecraft is hampered by the low spectral resolution and limited number of spectral bands, typically less than 10 bands of 100 to 200 nm width. Imaging spectrometry in remote sensing concerns the acquisition of image data in many narrow (< 40 nm wide) contiguous spectral bands with the ultimate goal of producing detailed spectral reflectance curves for each pixel in the image. Many minerals and rocks have unique spectral signatures with characteristic absorption features that are 20 to 40 nm wide. Imaging spectrometers allow to depict these narrow features and thus map surface mineralogy based on spectral image characterization. This paper gives a review of imaging spectrometry and addresses the following topics: airborne and spaceborne systems available, spectral and geometric data pre-processing, atmospheric correction, techniques for thematic data analysis, and applications in the field of geological remote sensing. In the final section a case study is described where imaging spectrometer data is used for mapping surface mineralogy in a hydrothermal alteration system, thus guiding gold exploration.

Introduction

When light interacts with a mineral or rock, certain wavelengths are preferentially absorbed while at other wavelengths light is transmitted in the substance. Reflectance, defined as the ratio of the intensity of light reflected from a sample to the intensity of the light incident on it, is measured by reflection spectrophotometers which are composed of a light source and a prism to separate light into different wavelengths. The separated light beams interact with the sample and the intensity of reflected light of various wavelengths is measured by a detector relative to a reference standard of known reflectance. Thus, a continuous reflectance spectrum of the sample is obtained.

Reflectance spectra have been used for many years to obtain compositional information of the Earth's surface. Similarly, it has been shown that spectral reflectance in visible and near-infrared offers a rapid and inexpensive technique for determining the mineralogy of samples and obtaining information on chemical composition. Electronic transition and charge transfer processes (e.g. changes in energy states of electrons bound to atoms or molecules) associated with ions of transition metals such as Fe, Ti and Cr, largely determine the position of diagnostic absorption features in the spectra of minerals (Burns 1970, Adams 1974, 1975). In addition, vibrational processes in H_2O and OH^- (e.g. small displacements of the atoms about their resting positions) produce fundamental overtone absorptions (Hunt 1977, Hunt & Salisbury 1970). Electronic transitions produce broad absorption features that require higher energy levels than do vibrational processes, and therefore take place at shorter wavelengths (Hunt 1977, Goetz 1991). The position, shape, depth, width, and asymmetry of these absorption features are controlled by the particular crystal structure and chemical composition of the absorbing mineral. Thus, variables characterizing absorption features can be directly related to the mineralogy of the sample.

The reflectance spectra of minerals are well known (e.g. Clark et al. 1990a, Grove et al. 1992) and several studies have been conducted to determine reflectance spectra of rocks (Hunt et al. 1973 and articles in following issues of the same journal). The reflectance characteristics of rocks can be simulated accurately by studying the compound effect of the reflectances of minerals in a spectral mixture forming the rock. Reflectance spectra of mineral mixtures are a systematic combination of the reflectances of the pure mineral components or end-members in the mixtures. Several investigators have examined the systematics of mixing theoretically and empirically, and found that if the scale of mixing is large, or macroscopic, the spectral systematics of mixing different materials are linear while for microscopic or intimate mixtures the systematics are nonlinear (Nash & Conel 1974, Singer 1981). Mathematical models for the analysis of reflectance spectra of mineral mixtures and rocks have been presented by many workers.

Reflectance spectra of minerals measured by different spectroradiometers with different spectral resolution are stored in spectral libraries that are available in digital format (e.g. Grove et al. 1992, Clark et al. 1990a). Similar spectral libraries are available for vegetation (e.g. Elvidge 1990) and soils (e.g. Baumgardner et al. 1985, Condit 1970).

Remote sensing of the surface of the Earth from aircraft and from spacecraft provides information not easily acquired by surface observations. Until recently, the main limitations of remote sensing were that no subsurface information could be obtained and that surface information lacked detail due to the broad bandwidth of scanners available. It has been shown that orbital imaging radar can provide subsurface data in arid regions (McCauley et al. 1982), and work on high-spectral resolution radiometry has shown that earth surface mineralogy can be identified using spectral information from scanner data (Goetz et al. 1982). Conventional sensors (e.g. Landsat MSS and TM, and SPOT) acquire information in a few separate spectral bands of various widths (typically in the order of 100 to 200 nm), thus smoothing to a large extent the reflectance characteristics of the surface (Goetz & Rowan 1981). Most terrestrial materials are characterized by spectral absorption features typically 20 to 40 nm in width (Hunt 1980). New scanner types were developed which acquire data in many small contiguous wavelength bands, allowing laboratory-like reflectance spectra to be produced for each pixel in the image. The field of imaging spectrometry, dealing with 'the acquisition of image data in many contiguous spectral bands' (Goetz 1991), is concerned with analysing such scanner data.

This paper describes the use of imaging spectrometer data for geological applications by describing the processing chain of data analysis from the raw data acquisition all the way up to the prospective applications. In the next sections the following topics are addressed:

- airborne and spaceborne instruments,
- data acquisition and (spectral, spatial, noise adjustment) pre-processing,
- radiance to (absolute and relative) reflectance correction,
- data analysis techniques,
- geological applications; case study.

Airborne imaging spectrometer systems

The first publicly available airborne spectrometer data were collected in 1981 using a one-dimensional profile spectrometer developed by the Geophysical Environmental Research Company which acquired data in 576 channels covering the 0.4–2.5 μm wavelength range (Chiu & Collins 1978) followed by the Shuttle Multispectral Infrared Radiometer (SMIRR) in 1981. The first imaging device was the Fluorescence Line Imager (FLI; also known as the Programmable Line Imager, PMI) developed by Canada's Department of Fisheries and Oceans in 1981, followed by the Airborne Imaging Spectrometer (AIS) developed at the NASA Jet Propulsion Laboratory which was operational from 1983 onward. This instrument acquired data in 128 spectral bands in the range of 1.2 to 2.4 μm with a field-of-view of 3.7° resulting in images of 32 pixels width (Vane & Goetz 1988). A later version of the instrument, AIS-2, covered the 0.8 to 2.4 μm region acquiring images of 64 pixels. In 1987 NASA issued an improved version of AIS called the Airborne Visible/Infrared Imaging Spectrometer (AVIRIS; Vane et al. 1993). While AIS was a prototype, AVIRIS was proposed as a facility that would routinely supply well-calibrated data for many different purposes. The AVIRIS scanner makes possible the simultaneous collection of images in 224 contiguous bands resulting in a complete reflectance spectrum for each 20 by 20 m pixel in the 0.4 to 2.5 μm region with a sampling interval of 10 nm (Goetz et al. 1982, Vane & Goetz 1988, 1993). The field-of-view of the AVIRIS scanner is 30° resulting in a ground field-of-view of 10.5 km. Private companies ever since recognized the potential of imaging spectrometry resulting in several sensors

Table 1. A selection of airborne imaging spectrometer systems currently operational for geological remote sensing (after: Staenz 1992). For an update consult:
http://www.eol.ists.ca/documents/IS-Team-Canada/

Sensor	*N*	Spectral coverage (nm)	Band width (nm)	GIFOV (mrad)
AHS	48	440 – 12700	20–1500	2.5
AMSS	32	490 – 1090	20–71	2.1 or 3.0
	8	2020 – 2370	60	
	6	8500 – 12000	550–590	
ARES	75	2000 – 6300	25–70	1.17
AVIRIS	224	400 – 2450	9.4	1
DAIS 7915	32	498 – 1010	16	3.3, 2.2, 1.1
	8	1000 – 1800	100	
	32	70 – 2450	15	
	1	3000 – 5000	2000	
	6	8700 – 12300	600	
GERIS	24	400 – 1000	25.4	2.5, 3.3, 4.5
	7	1000 – 2000	120	
	32	2000 – 2500	16.5	
HYDICE	206	400 – 2500	7.6–14.9	0.5
ISM	64	800 – 1700	12.5	3.3, 11.7
	64	1500 – 3000	25	
MAIS	32	450 – 1100	20	3, 4.5
	32	140 – 2500	30	
	7	8200 – 12200	400–800	
MIVIS	20	433 – 833	20	2.0
	8	1150 – 1550	50	
	64	2000 – 2500	8	
	10	8200 – 12700	400–500	
SFSI	120	1200 – 2400	10	0.33

N = number of bands; GIFOV = ground instantaneous field of view.

for specific applications. Examples are the GER imaging spectrometer that became operational in 1986 and the ITRES CASI that became operational in 1989. Currently many space agencies and private companies in developed and developing countries operate there own instruments. An overview is given in Table 1.

Future planned spaceborne imaging spectrometer systems

A number of orbital imaging spectrometer missions are planned or being prepared currently. HIRIS, the High Resolution Imaging Spectrometer (Goetz & Herring 1989, Kerekes & Landgrebe 1991) is designed to acquire images in 192 spectral bands simultaneously in the 0.4 to 2.5 μm wavelength region with a ground resolution of 30 m and a swath width of 30 km. This scanner has a spectral resolution of 9.4 nm in the 0.4 to 1.0 μm wavelength region and an 11.7 nm spectral resolution in the 1.0 to 2.5 μm wavelength range. Though an interesting design, it seems unlikely that the HIRIS will ever be built after the budget cuts at NASA after the Challenger accident. NASA is now supporting instead the Advanced Spaceborne Thermal Emission and Reflectance Radiometer (ASTER; Kahle et al. 1991), a high-spectral-resolution imaging spectrometer planned for 1999. The instrument is designed with three bands in the visible and near-infrared (VNIR) spectral range with a 15 m spatial resolution, six bands in the short-wave infrared (SWIR) with a 30 m spatial resolution, and five bands in the Thermal infrared with a 90 m spatial resolution. The VNIR and SWIR bands have a spectral resolution in the order of 10 nm. Simultaneously, a single band in the near-infrared will be provided for stereo capability. The swath width of an image will be 60 km with 136 km crosstrack and a temporal resolution of 16 days. The European Space Agency (ESA) is developing two spaceborne imaging spectrometers (Rast 1992): The Medium Resolution Imaging Spectrometer (MERIS) and the High Resolution Imaging Spectrometer (HRIS; now renamed to PRISM, the Process Research by an Imaging Space Mission). MERIS, currently planned as payload for the satellite Envisat-1 (see also http://www.esoc.esa.de/external/mso/envisat.html) to be launched in July 1999 with the Ariane 5, is designed mainly for oceanographic application and covers the 0.39 to 1.04 μm wavelength region with 1.25 nm bands at a spatial resolution of 300 or 1200 m (Rast & Bézy 1995). PRISM, currently planned for Envisat-2 to be launched around the year 2000, is a spectrometer similar to HIRIS which will cover the 0.4 to 2.4 μm wavelength range with a 10 nm contiguous sampling interval at a 32 m ground resolution. The first satellite imaging spectrometer expected was the LEWIS Hyperspectral Imager (HSI), however, ground communication with the instrument was lost a few hours after launch in July 1997. A few days later the satellite returned to Earth and burned in the atmosphere. Several instruments are in the design stage such as the Chinese CIS which will have 36 bands in the visible to shortwave-infrared wavelength region and the NASDA GLI. Another initiative is the Australian (e.g. CSIRO) ARIES with 32 bands from 500 to 1000 nm and 32 bands from 2000 to 2500 nm which is in the planning stage.

Data acquisition and pre-processing of imaging spectrometer data

Acquisition and pre-processing are generally conducted by the manufacturers or the institute or agency that maintains and operates the instrument. In most cases the user is provided with at-sensor radiance data and the necessary instrument characteristics (e.g. spectral response functions, band passes) needed for further analysis. Here the following pre-processing steps are described:

- spectral calibration,
- spatial calibration,
- noise adjustment.

The following sections are derived from discussions with engineers and scientists involved in the calibration of airborne imaging spectrometers, a subject poorly covered in literature. Those seeking more details are referred to the following articles and book chapters: data acquisition (Goetz 1992), spectral calibration (Green 1992, Green et al. 1988a), geometric calibration and geocoding (Meyer 1994), and signal-to-noise calculation (Gao 1993, Curran & Dungan 1989).

The spectral pre-processing chain

Data acquisition – Data acquisition by imaging spectrometers can be done using the whiskbroom or pushbroom principle. In the whiskbroom configuration a mirror scans cross-track (i.e. perpendicular to the direction of platform movement), and radiation from each pixel is projected through an optical system onto a line array of detector elements that are sensitive for the wavelength range covered by the scanner. Thus, each pixel is viewed separately which allows a wide field of view and only one detector in each spectral band to be calibrated. The disadvantage is the short dwelling time (the time that the instrument ‘sees’ each pixel) which limits the spatial and spectral resolution as well as the ratio of signal versus noise. Furthermore, the rotating mirror often causes resonance that may be observed in the data as striping. Opposed to the whiskbroom principle is the pushbroom principle of data acquisition in which two-dimensional area arrays are used with one dimension giving again the spectral wavelength range and the other dimension one scan-line of pixels. This type of scanner has no moving parts and a longer dwell time on each pixel yielding a better signal versus noise ratio. However, each of the ten-thousand detectors on the array have to be calibrated individually which has been shown to be time consuming.

Analog to digital conversion – Incoming light or radiation from the surface is split by beam splitters into the wavelength ranges specified by the instrument. By means of a set of lenses, the incoming photons are projected onto the array containing light-sensitive elements on which the charge accumulating is proportional to the integrated light intensity. For signal read-out, the charges accumulated on the detector elements are passed through an amplifier and a digitizer for analogue to digital conversion. This results in a digital signal, referred to here as raw radiance, digitized in 8, 12 or 16 bits. Detector materials currently used are silicon for the 400 to 1000 nm, lead sulfide for the 800 to 2500 nm and indium antimonide for the 800 to 5000 nm range.

Geometric spectral calibration – Spectral response is not homogenous when measured over the area covered by a pixel. The point-spread function describes the decline of the measured signal and is found using a monochromator covering the sensor-designated wavelength coverage and different pinhole targets.

Spectrometric calibration – Similar to the point-spread function it can be shown that for each spectral channel that the sensor acquires the radiance is variable. Rather than a channel sensing only photons of one particular wavelength, the channel measures radiance in a wavelength range that stretches from a few nanometers lower and a few nanometers higher than the central wavelength of the channel. The curve describing the (gaussian) decline of the radiance levels around the central channel wavelength for each channel is known as the spectral response function which can again be deduced by experimenting with a monochromator.

Radiometric calibration – Imaging spectrometers take indirect measurements of physical parameters in the sense that the digitized signal recorded is directly proportional to the incoming photon energy but not in any physically meaningful unit. The relation between the raw digitized signal and a physical meaningful parameter is established after radiometric correction yielding spectral radiance measured as the photon flux power per unit solid angle per wavelength interval. During radiometric calibration the radiometric response function is derived which defines the relation between the signal, caused on the detectors by the bombardment by photoelectrons, and the incoming radiance. This function allows to translate all raw radiance into spectral radiance. The analysis in carried out by mounting the sensor onto a so-called integrating sphere, a half circular reference coated with highly reflective barium sulfate and isolated from daylight. A set of lamps allows to produce light of known spectral radiance in the integrating sphere which can be compared with the measurements of the sensor. These are cross-calibrated using a field spectroradiometer with known standard radiance. The radiometric response function corrected for the spectral response and geometric response as well for the temporal response (not further elaborated here) gives the at-sensor spectral radiance.

Spatial pre-processing chain

Aircraft data suffer from spatial distortions related to the carrier movements and the ruggedness of the terrain. Modern aircraft remote-sensing campaigns are flown with onboard DGPS for absolute location of the aircraft at acquisition time and with onboard gyros that record tilt of the aircraft in terms of roll, pitch and yaw. In geometric correction, for each pixel the original observation geometry is reconstructed based on the flight line, aircraft altitude, surface topography and aircraft navigational information. The result of the correction is geocoded at-sensor radiance data. Usually, this geometric correction of aircraft imaging spectrometer data is not included in the standard data products, but will only be executed on request.

Noise adjustment

Signal in imaging spectrometry is considered to be the quantity measured by an imaging spectrometer sensor, whereas noise describes the random variability of the signal. The quantification of the noise level alone is not a very useful measure for the quality of an imaging spectrometer data set since the effect is more severe when signal is low. Therefore, in most studies the signal-to-noise ratio is used; the ratio of the signal's mean to its standard deviation is used as an estimate. Imaging spectrometer data sets contain both periodic (coherent) sensor noise that can be removed and random noise that cannot. The signal-to-noise calculation is carried out on data sets with periodic noise removed. The remaining random noise can be additive noise, which is independent of the signal, and multiplicative noise which is proportional to the signal. The major part of the noise in imaging spectrometer data sets is additive and decreases sharply with increases in wavelength and atmospheric absorption. This random noise component consists of random sensor noise (which is image independent), intra-pixel variability (resulting from spatially heterogeneous pixel contents), and interpixel variability.

An increase in signal to noise ratio can be obtained by reducing the noise and retaining the signal. A method for doing so is the Minimum Noise Fraction (MNF) transform developed by Green et al. (1988b). The MNF algorithm is a method for ordering data cubes into components of image quality using a cascaded principal components transform that selects new components in order of decreasing signal-to-noise ratio. In this approach, the grey levels are considered linear combinations of an uncorrelated signal component and a correlated noise component in which the grey level covariance is the sum of the signal and the noise matrices. The difficulty in applying the MNF technique lies in finding these covariance matrices. The grey level covariance matrix can be readily derived as the sample covariance matrix of the data. However, the noise covariance matrix is more complex to assess. Green et al. (1988b) showed that estimating the noise covariance matrix is unnecessary when noise occurs in one band only. These authors developed a procedure known as Minimum/Maximum Autocorrelation Factors (MAF) to estimate the noise covariance matrix for more complex cases. MAF exploits the fact that in most remote sensing data the signal at any pixel is strongly correlated with the signal at neighbouring pixels, while the noise is not. The original data are transformed into linear orthogonal combinations in order of increasing spatial correlation which can be subsequently treated. The common approach is to apply low-pass filtering to the low-order MAF factor images which contain most of the low spatially correlated noise and a degraded signal component, and removal of the high-order MAF factor images that contain nearly only noise. After filtering, the cleaned MAF factor images are backtransformed to the original data space.

Radiance to reflectance correction

Atmospheric disturbance

Raw imaging spectrometer data have the general appearance of the solar irradiance curve, with radiance decreasing towards longer wavelengths, and exhibit several absorption bands due to scattering and absorption by gasses in the atmosphere. The major atmospheric water vapour bands are centred approximately at 0.94, 1.14, 1.38 and 1.88 μm, the oxygen band at 0.76 μm, and carbon dioxide bands near 2.01 and 2.08 μm. Additionally, other gasses including ozone, carbon monoxide, nitrous oxide, and methane, produce noticeable absorption features in the 0.4 to 2.5 μm wavelength region. The effect of atmospheric calibration algorithms is to re-scale the raw radiance data provided by imaging spectrometers to reflectance by correcting for atmospheric influence thus shifting all spectra to nearly the same albedo. The result is a data set in which each pixel can be represented by a reflectance spectrum which can be directly compared to reflectance spectra of rocks and minerals acquired either in the field or in the laboratory. Reflectance data obtained can represent absolute radiant energy or apparent reflectance relative to a certain standard in the scene. Comparison of several methods for radiance to reflectance correction can be found in Rast et al. (1991), Roberts et al. (1985) and Van der Meer (1994a). Calibration to reflectance can be conducted to result in absolute or relative reflectance data.

Absolute reflectance

Absolute reflectance data without a priori knowledge of surface characteristics can be obtained using atmosphere models. These models correct for scattering and absorption in the atmosphere due to water vapour and mixed gases as well as for topographic effects and different illumination conditions. The 940 nm and 1100 nm water absorption bands are used to calculate water vapour in the atmosphere while transmission spectra of the mixed gases in the 400 to 2500 nm wavelength region are simulated on the basis of the water-vapour values found and the solar and observational geometry. Scattering effects in the atmosphere are modeled using radiative transfer codes such as LOWTRAN and its successor MODTRAN (U.S. Air Force Geophysics Lab.) and 6S (University of Lille). In essence, radiative transfer codes quantitatively model the difference between the radiation leaving the earth and the radiation received at the sensor, using scattering and transmission properties of the atmosphere. Radiative transfer codes have typical atmosphere models for a large number of atmosphere types that allows to calculate an atmospheric radiance spectrum on a pixel-by-pixel basis. The surface reflectance is obtained by dividing the at-sensor radiance by the model solar irradiance. Through this atmospheric correction, a geocoded reflectance image data set is obtained (e.g. Richter 1996a, b, Zagolski & Gastellu-Etchegorry 1995).

Relative reflectance

In relative reflectance data, reflectivity is measured relative to a standard target from the scene. Correction methods currently available for this purpose include:

- flat field correction,
- internal average relative reflectance correction,
- empirical line correction.

Flat-field correction method – The purpose of the flat-field correction is to reduce the atmospheric influence in the raw imaging spectrometer data and to eliminate the solar irradiance drop-off, as well as any residual instrument effects. This is achieved by dividing the whole data set by the mean value of an area within the scene which is spectrally and morphologically flat, and spectrally homogeneous. The flat-field chosen should have a high albedo to avoid decrease of the signal-to-noise ratio. This can also be achieved by increasing the number of pixel spectra used to produce the flat-field spectrum. In order to properly select a flat-field target area, ground truth data is necessary to ensure that the calibration target is indeed spectrally flat. In that case, the flat-field method removes the solar irradiance curve and major gaseous absorption features as well as system induced defects.

Internal average relative reflectance correction method – The internal average relative reflectance (IARR) correction method allows the calibration of raw imaging spectrometer data to reflectance data when no calibration information is available (Kruse et al. 1985, Kruse 1988, Ben-Dor & Kruse 1994). This procedure uses an 'average reference spectrum' calculated as the average pixel spectrum of the entire scene. The radiance spectrum of each pixel is divided by this average spectrum to produce a relative reflectance spectrum. Care should be taken when types of surface cover with strong absorption features are present in the scene. In such a case the IARR correction method may cause artefacts which could be wrongly interpreted as spectral features.

Empirical line method – Conversion of raw imaging spectrometer data to reflectance data using the empirical line method (Kruse et al. 1985, 1990, Kruse 1988) requires the selection and spectral characterization of two calibration targets (Roberts et al. 1985), thus assuming a priori knowledge of each site. This empirical correction uses a constant gain and offset for each band in order to force a best fit between sets of field spectra and image spectra characterising the same ground areas, thus removing atmospheric effects, residual instrument artefacts and viewing geometry effects. The correction requires four basic steps (Kruse et al. 1990), consecutively:

1) To choose two ground target regions with a wide albedo range (e.g. a dark and a bright target) and acquiring field spectra characterising these targets.
2) To select multiple pixels that are associated with each of the two ground targets.
3) To construct an over-determined system of linear equations for each band in which the gain and offset values are the unknown values and the number of knowns is equal to the total number of image pixels chosen. Solving these equations by means of least squares fitting provides gain and offset spectra and a standard error for these values for each parameter at each wavelength. The gain spectrum is an inverse solar irradiance curve, whereas the offset spectrum is a negative correction factor that increases with wavelength.
4) To actually calibrate the data, multiply the instrument raw digital numbers by the proper gain factor, adding the corresponding offset value.

Thematic analysis techniques for absorption feature extraction

Now that reflectance-like imaging spectrometer data is obtained, the next step is to map absorption features to make positive discrimination of surface reflectance targets. A large number of techniques have been designed to enable this:

- binary encoding,
- waveform characterization,
- spectral feature fitting,
- spectral angle mapping,
- spectral unmixing,
- constrained energy minimization,
- classification,
- cross correlogram spectral matching.

Binary encoding – In binary encoding, pixel spectra are encoded such that the result is a one-zero representation of the brightness of a pixel in various spectral bands using a threshold level equal to the average brightness of the pixel over all channels. A simple binary code for a reflectance spectrum can be described as (Goetz et al. 1982):

$$h(\mathbf{n}) = 0 \text{ if } x(\mathbf{n}) \leq T \text{ and } h(\mathbf{n}) = 1 \text{ if } T < x(\mathbf{n}),$$

where $x(\mathbf{n})$ is the brightness value of a pixel in the **n**th channel, T is the user-specified threshold which often equals the average brightness value of the spectrum, and $h(\mathbf{n})$ is the resulting binary code for the pixel in the **n**th band. A modification to the simple encoding has been proposed by Jia & Richards (1993) who exploit multiple thresholds. Their method consists of determining the mean brightness of a pixel vector and then setting additionally upper and lower thresholds.

Waveform characterization – In waveform characterization (Okada & Iwashita 1992), first the imaging spectrometer data are normalized to produce reflectance-type images. The upper convex 'Hull' is calculated as an enveloping curve on the pixel spectra. This Hull (also referred to as 'continuum') is essentially a mathematical function used to isolate absorption features from background signal. The Hull or continuum removal uses local maxima on the spectrum which are connected by line segments. Dividing the Hull into the original spectrum results in its removal, thus leaving only absorption features to remain (Clark & Roush 1984, Green & Graig 1985). These Hull-removed spectra are used to characterize absorption features, known to be attributed to a certain mineral of interest, in terms of their position, depth, width, asymmetry, and slope of the upper convex Hull. As a result of the waveform characterization, five images (e.g. position, depth, width, symmetry, and slope of upper Hull image for each absorption feature) can be generated defining the similarity between a pixel spectrum and a laboratory spectrum of a mineral of interest. The similarity is based on the presence of characteristic absorption features in both spectra. However, Okada & Iwashita (1992) give no solution to the mineral mapping from these images. Techniques need to be developed to quantitatively estimate the probability of a mineral occurrence from the waveform characteristics.

Spectral feature fitting – Spectral feature fitting builds on waveform characterization in that it is an absorption feature-based method for matching image spectra to laboratory spectra (Crowley et al. 1989, Clark et al. 1990b, Crowley & Swayze 1995). Again continuum-removed pixel spectra are used and compared to continuum reference spectra of known mineralogy, possibly derived from a spectral library. A least-squares fit is calculated band by band between each reference end member and the unknown pixel spectra. The root mean square (RMS) error of this fit is used to create an RMS image that shows pixels that are more, and pixels that are less similar to the selected reference end member.

Spectral angle mapping – Spectral angle mapping (Kruse et al. 1993) calculates the spectral similarity between a test reflectance spectrum and a reference reflectance spectrum assuming that the data is correctly calibrated to apparent reflectance with dark current and path radiance removed. The spectral similarity between the test (or pixel) spectrum and the reference (or laboratory) spectrum is expressed in terms of the average angle between the two spectra. In this approach, the spectra are treated as vectors in a space with dimensionality equal to the number of bands. The outcome of the spectral angle mapping for each pixel is an angular difference measured in radiance ranging from zero to $\pi/2$ which gives a qualitative estimate of the presence of absorption features which can be related to mineralogy.

Spectral unmixing – Spectral unmixing is based on the assumption that a pixel is composed of the spatial mixing of materials within the area bounded by the pixel. Each material has a characteristic spectral signature. Together these signatures result in the reflected electromagnetic radiation observed in imaging spectrometer data. These spectrally pure end-member materials have to be identified and their spectra have to be known in the same band configuration as the imaging spectrometer data. In simplified form, spectral unmixing assumes a linear relationship between an observed spectrum and a library composed of end-member spectra given in matrix form as $\mathbf{A} * \mathbf{X} = \mathbf{B}$ and thus by inversion $\mathbf{X} = \mathbf{A}^{-1} * \mathbf{B}$ where $\mathbf{A}$ is an M by N end-member library matrix, $\mathbf{X}$ is an N by 1 abundance vector, and $\mathbf{B}$ is an M by 1 observed data vector with M as the total number of bands and N the total number of mixing end members. The end-member library matrix and the observed pixel spectrum are known and the abundance values are unknown, thus the equation can be solved by means of a least squares approximation if the number of end members is equal to the number of spectral bands minus one (or less). Finally, the sum of the abundances for each known end member is calculated on a pixel-by-pixel basis together with the root-mean-squared error of fit between the observed mixed pixel spectrum and the theoretically derived mixed spectrum from the abundances of the end members and their respective spectra. The RMS error image displays how well the mixing library can be used to model each observed spectrum, and can thus be used to assess the validity of the end-member spectra. Selection of end members can be done using 1) ‘known’ end members drawn either from areas in the scene where ground knowledge is available or from a spectral library, or 2) ‘derived’ end members that are extracted by a statistical method from the data cube without prior knowledge. A commonly used method for finding spectrally pure pixels in a data set is the pixel purity index (PPI; Boardman et al. 1995). This index is found by repeatedly projecting n-dimensional scatter plots onto a random unit vector. The extreme pixels in each projection are recorded and the total number of times each pixel is marked is noted. This number is displayed in an image in which brighter pixels represent more spectrally extreme materials. Reviews of linear and non-linear approaches to spectral unmixing are given in Settle & Drake (1993) and Ichoku & Karnieli (1996).

Constrained energy minimization – Constrained energy minimization (CEM), developed by Farrand & Harsanyi (1997), is an extension to spectral unmixing. It maximizes on a pixel-by-pixel basis the response of a target signature and suppresses the response of undesired background signatures. It is assumed that foreground and background signatures are mixed linearly such as is the case when each photon only interacts with one material. The CEM strives at finding a vector that suppresses the unknown background signature while enhancing the target signature. This is achieved by minimizing the total output energy of all pixels and by assuming the energy of an individual pixel summed across the wavelength range to be 1 when applied to the a target pixel spectrum. The result of CEM is a vector component image that is comparable to fraction abundance images, typically obtained through unmixing.

Classification – Classification of remotely sensed imagery into groups of pixels having similar spectral reflectance characteristics is often an integral part of digital image analysis. The spectral reflectance of so-called training pixels (i.e. pixels known to represent a ground class of interest) are used to classify pixels for which the ground cover type is unknown. Classification routines thus aim at comparing the observed spectral reflectance of pixels of unknown composition with that of training pixels, and assign the unknown pixel to that group which most resembles its spectral reflectance characteristics. Techniques making use of training data sets are referred to as supervised classification algorithms as opposed to unsupervised classification techniques in which no foreknowledge of the ground classes is required. Supervised and unsupervised image classification techniques have been widely used in the analysis of conventional remote sensing data (e.g. Landsat MSS and TM, and SPOT) and several studies have been undertaken to develop algorithms based on the classification of hyper-spectral data types. Cetin et al. (1993) and Cetin & Levandowski (1991) use n-dimensional probability density functions based on the principle of the maximum likelihood classifier to analyse AVIRIS, TIMS, and Landsat TM images. Lee & Landgrebe (1993) give algorithms for the minimum distance classifier in high-spectral resolution imagery. An approach using neural networks is given in Benediktsson (1995). An alternative classification algorithm for imaging spectrometer data based on indicator kriging is given in Van der Meer (1994b, 1996a).

Cross correlogram spectral matching – Cross correlogram spectral matching (CCSM; Van der Meer & Bakker, 1997a, b) is a new approach toward mineral mapping from imaging spectrometer data using the cross correlogram of pixel and reference spectra. A cross correlogram is constructed by calculating the cross correlation at different match positions, M, between a test spectrum (i.e. a pixel spectrum) and a reference spectrum (i.e. a laboratory mineral spectrum or a pixel spectrum known to represent a mineral of interest) by shifting the reference spectrum over subsequent channel positions by:

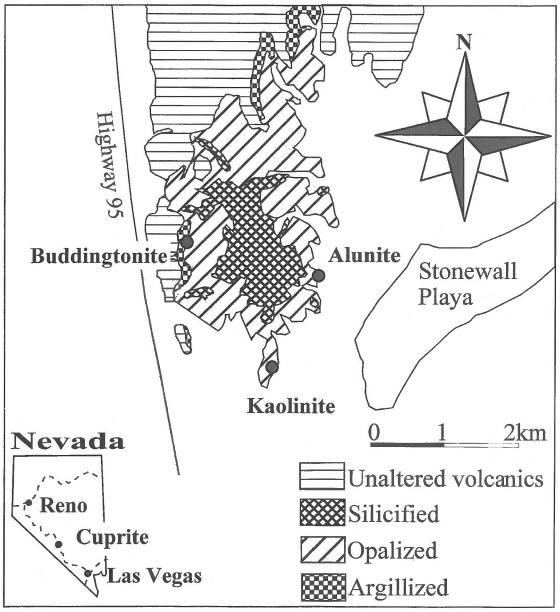

Figure 1. Alteration map of volcanics in Cuprite mining district, Nevada (unpublished data, Nevada State Geol. Survey). •: Locations shown in Figure 2.

$$r_M = \frac{N\Sigma\lambda_r\lambda_t - \Sigma\lambda_r\Sigma\lambda_t}{\sqrt{[N\Sigma\lambda_r^2 - (\Sigma\lambda_r)^2][N\Sigma\lambda_t^2 - (\Sigma\lambda_t)^2]}},$$

where r_M is the cross correlation at match position M, λ_t is the test spectrum, λ_r is the reference spectrum, N is the number of overlapping positions (spectral bands), and M the match position. The statistical significance of the cross correlation coefficient can be assessed by a Student's t-test and the skewness can be calculated as an estimator of the goodness-of-fit. The cross correlogram for a perfectly matching reference and test spectrum is a parabola around the central matching number ($M = 0$) with a peak correlation of 1. Deviations from this shape indicate a different surface mineralogy. Mineral mapping on a pixel-by-pixel basis is achieved by extracting three parameters from the cross correlograms and combining these into a statistical estimate of the goodness of fit of the two spectra compared: the correlation coefficient at match position zero, the moment of skewness (based on the correlation differences between match numbers of equal but reversed signs, e.g. $M = 4$ and $M = -4$), and the significance (based on a Student t-test testing the validity of the correlation coefficient at $M = 0$). In order to evaluate the surface mineralogy maps an RMS error assessment procedure is proposed in Van der Meer &

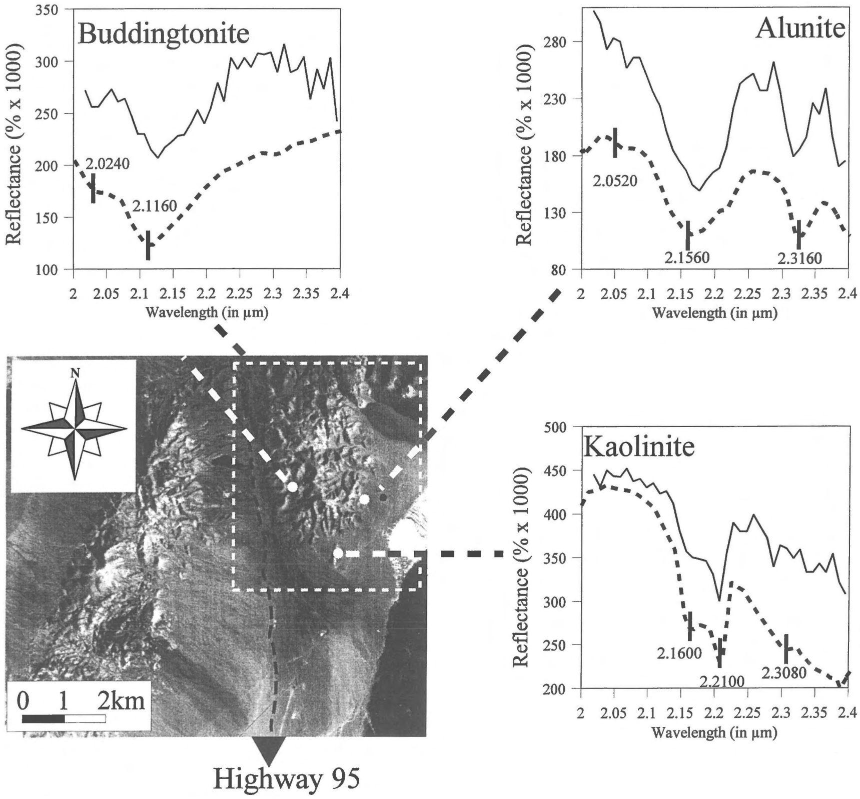

Figure 2. AVIRIS band 180 centred at 2.06746 μm of Cuprite mining district, with locations (○) of known outcrops of kaolinite, alunite and buddingtonite. Box outlines area of Figure 4. Single-pixel AVIRIS spectra (solid lines) and corresponding laboratory reflectance spectra (dashed lines) are shown in the graphs, while vertical bars indicate centre positions (wavelength indicated) of absorption features characterizing these minerals.

Bakker (1998) in which the error is calculated from the difference between the calculated pixel cross correlogram and the ideal cross correlogram calculated for the reference as:

$$\mathrm{RMS} = \sqrt{\frac{\Sigma_0^M (r_M - r'_M)}{N}},$$

where r_M is the pixel cross correlation at match position M, r'_M is the reference cross correlation at match position M, N is the number of match positions, and M is the match number.

Applications of imaging spectrometry

Numerous examples can be given where imaging spectrometer data have been used for surface mineralogy mapping based on quantitative comparison of unknown pixel spectra and laboratory spectra of minerals (e.g. Abrams & Hook 1995, Bowers & Rowan 1996). Many of these studies focus on mapping hydrothermal alteration as a guide to mineral exploration (e.g. Ferrier & Wadge 1996). Other alteration processes that have been studied in imaging spectrometer data are the serpentinization of ultramafic rocks which relates to major asbestos deposits. Based on laboratory studies of Hunt & Evarts (1981) it has been show that the degree of serpentinization of ultramafic rocks can be estimated through spectral analysis of imaging spectrometer data (Van der Meer 1995).

Indirect detection of mineral deposits using imaging spectrometer data has been attempted through analysis of spectra of 'stressed vegetation'. Collins et al. (1983) were the first to report the shift of the red edge toward the blue end of the spectrum as a result of vegetation stress due to copper in the subsurface. These authors claimed that the position and shape of the red edge could be used to guide mineral prospecting. Their work has led to a still ongoing debate on the potential use of the red-edge shift. Although the amount and direction of shift as a result of geochemical stress on vegetation is uncertain, most workers agree that the red edge can be used to assess the vitality of plant communities (see Boochs et al. 1990 for a discussion on this topic). Similarly, Lehmann et al. (1990) investigated spectra of a vegetation-covered mine-waste deposit.

Alternatively, geological imaging spectrometry may be used to assist metamorphic facies mapping for regional geological investigations (e.g. Rowan et al. 1987, Van der Meer 1996b).

Through the analysis of the position of the absorption band in the 2300 nm wavelength range it has been shown that mapping calcite versus dolomite is possible from imaging spectrometer data, thus allowing to map dolomitization patterns from space (Windeler & Lyon 1991). This has potential for petroleum exploration since increases of porosity due to dolomitization may give rise to reservoir rocks.

Some studies have been undertaken to attempt detection of hydrocarbon micro-seepages in remote-sensing data (e.g. Yang et al. 1999). Such seepages may be related to subsurface oil occurrences.

All studies mentioned so far use imaging spectrometer data calibrated to reflectance. As discussed previously, raw imaging spectrometer radiance data shows absorption features that can be attributed to atmospheric gases. Vice versa, these absorption features can be used to map quantities and differences in these gases in the atmospheric column. Using ratios of depths of water-absorption features at 950 and 1150 nm, it has been demonstrated that the 'water vapour total column abundance' can be mapped from imaging spectrometer data (Carrere & Conel 1993, Gao & Goetz 1990, 1995, Frouin et al. 1990). Similarly, De Jong (1998) detected abnormally high abundances of carbon dioxide and methane in AVIRIS data from the Mammoth Mountain area in California which they attributed to renewed volcanic activity.

An example of mineral mapping using cross correlograms

In this section, an example is given of surface-mineralogy mapping from imaging spectrometer data using cross correlogram spectral matching (CCSM). A cross correlogram is constructed by calculating the cross-correlation coefficient between a test spectrum (a pixel spectrum) and a reference spectrum (a laboratory or pixel spectrum known to characterize a mineral of interest) at different match positions. By convention, we move the reference spectrum and refer to a negative match position when shifting toward shorter wavelengths and to a positive match position when shifting toward a longer wavelength. Thus match position –1 means that we are calculating the cross correlation between the test spectrum and the reference spectrum in which all channels have been shifted by one channel position number to the lower end of the spectrum. The cross correlation at each match position, *m*, is equivalent to the linear correlation coefficient of the test and reference spectrum and is defined as the product of the covariance and the sum of the standard deviations. The statistical significance of the cross-correlation coefficient can be assessed by means of a *t*-test. To test the functionality of CCSM it has been applied to imaging spectrometer data from the AVIRIS flown at Cuprite (Nevada; Figure 1). Locations were marked of known occurrences of three minerals of interest: kaolinite, alunite and buddingtonite. AVIRIS single-pixel spectra from these locations were extracted from the data cube and compared with laboratory spectra of these minerals (Figure 2). These were subsequently used as reference spectra for the calculation of cross correlogram images. Pixel cross correlograms were calculated ranging from $M = 6$ to $M = -6$ to ensure that sufficient overlapping spectral channels were available to calculate a statistically meaningful correlation. For these cross correlogram

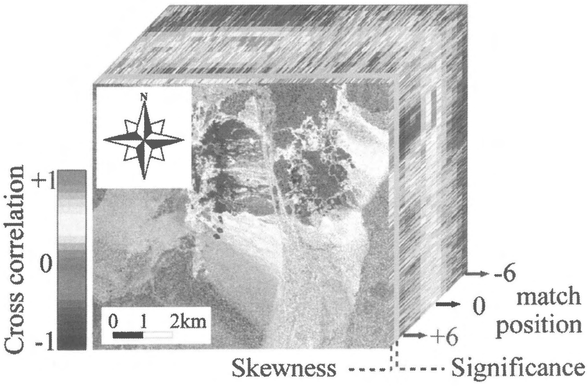

Figure 3. '3D' image correlogram cube for alunite. The face of the cube is a colour composite image of the area shown in Figure 2. (red = skewness; green = significance; blue = cross correlation at $M = 0$). Pixels similar to the mineral tested appear in white. The sides of the cube are spectral slices built up of cross correlogram images for the 13 match positions calculated. The correlation is coded using the colour scheme indicated by the bar (after Van der Meer & Bakker 1997b). (For full colour reproduction of this figure, see Appendix at the end of this issue.)

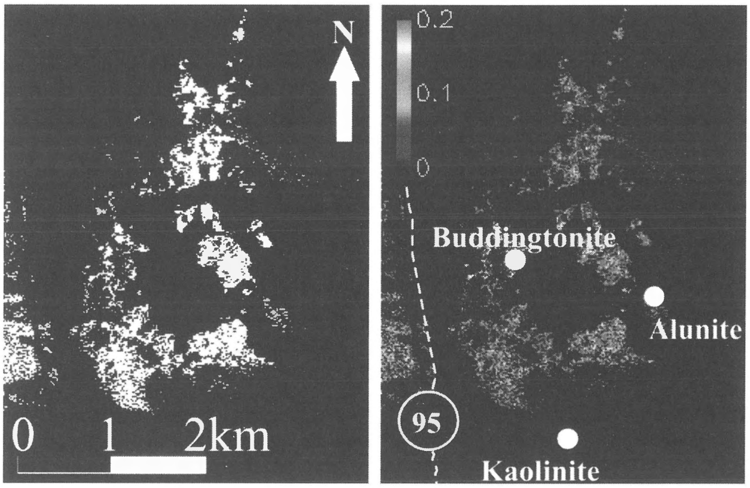

Figure 4. The image on the left shows the pixels classified as alunite in the northwestern part of the Cuprite mining district, using the cross correlogram spectral matching technique applied to AVIRIS data. The image on the right shows the root-mean-squared difference of the true and estimated pixel cross correlogram (after Van der Meer & Bakker 1998). See Figure 2 for location. (For full colour reproduction of this figure, see Appendix at the end of this issue.)

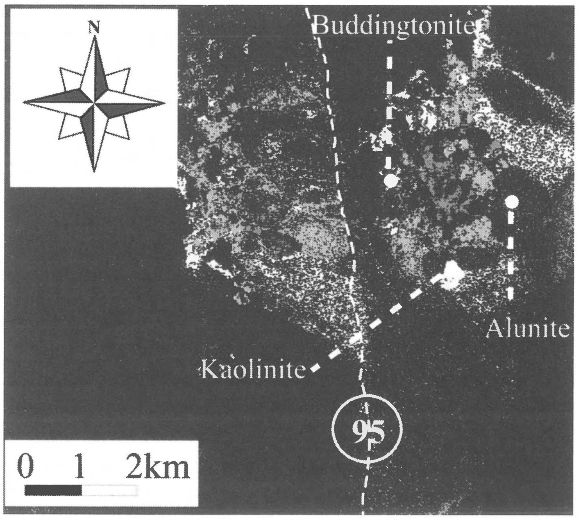

Figure 5. Final classification and alteration map for the Cuprite mining district, from AVIRIS data using the cross correlogram spectral matching technique. The scene is classified into kaolinite (yellow), alunite (cyan), silica (red) and buddingtonite (dark blue). Shown are pixels that have a cross correlation at $M = 0$, a skewness and a significance all exceeding 0.9 (after Van der Meer & Bakker 1998). (For full colour reproduction of this figure, see Appendix at the end of this issue.)

images the significance was calculated. The t-values for the thirteen cross correlation images were averaged and rescaled from 0 to 1 by dividing them by the value obtained at the reference pixel for kaolinite which was extracted from the AVIRIS data cube. By using an input spectrum from the data cube it was also possible to verify the validity of our results because at this location we expected (and also obtained) a perfect correlation of 1 at $M = 0$. Furthermore, the skewness of the pixel correlogram was calculated and also rescaled between 0 and 1. This was achieved by taking the absolute value of the sum of the correlation at $M = 4$ and $M = -4$ divided by 2 and subtracted from 1. Thus, pixels having a low skewness (i.e. a symmetric cross correlogram) have a rescaled value near to 1 while pixels with a skewed cross correlogram have values near to 0 on this scale. The resulting cross correlogram images and the significance and skewness images were combined into a single image data cube shown in Figure 3. The face of this ‘3D’ image cube is a colour-composite image with the skewness displayed in red, the significance displayed in green and the cross correlation at $M = 0$ displayed in blue. Pixels that appear white are mineralogically similar to the input reference spectrum whereas other colours may be interpreted through the contribution of the three components in the image. The sides of the cube are spectral slices corresponding to the top and right-hand side of the image. These spectral slices are formed by stacked cross correlation images for the 13 different match positions combined with the skewness and significance image. Each line in a slice thus represents a colour-coded pixel cross correlogram. Pixels that spectrally resemble the mineral spectrum tested, will have high correlation values at $M = 0$ appearing in red and low or negative values at $M = 6$ and $M = -6$ appearing in dark blue colours. The correlogram should ideally be symmetric and thus have a low skewness value represented in green colours. The cross correlogram image at $M = 0$, the skewness image and the significance image were used to produce a classification of the Cuprite AVIRIS data and to produce for each class an RMS image (Figure 4). The hydrothermal alteration zones as indicated by the aerial distribution of kaolinite, alunite and buddingtonite (Figure 5) compared favourably with results obtained by earlier investigations.

The mineral zonation as we mapped it at Cuprite is the result of a sulfuric acid-charged system with hydrothermal fluids emitted in a hot-spring type of environment. The circular distribution of the mineral zones demonstrates that alteration occurred along a central vent with the lateral mineral zoning controlled by decreases of acidity and temperature. The alunite in this zoning is a pathfinder mineral for gold deposits.

Conclusions

The acquisition of image data in many, narrow and contiguous spectral bands over the visible and shortwave-infrared wavelength region as is the case with imaging spectrometers provides detailed information on surface mineralogy not easily acquired by means of traditional field mapping. Current applications of imaging spectrometry are hampered by the limited availability of data. Since all data are acquired by aircraft, the accessibility is low due to the high costs involved in flying a system. However, several airborne campaigns have been conducted in the past and further planning of flight campaigns is ongoing. Another positive development is the interest that private companies show in this technology. This has brought up many instruments with specifications focused on certain applications. With the advent of spaceborne imaging spectrometer systems in the near future a continuation of current research is assured and application of the technology in geological exploration can be foreseen. Nevertheless, there is a need for aircraft data to allow further testing and fine tuning of algorithms to achieve this goal.

Acknowledgements

P. Strobl and D. Oertel of the Deutsche Forschungsanstalt für Luft- und Raumfahrt e.V. (DLR) and P.J. Curran of the University of Southampton are thanked for reviewing the manuscript.

References

Abrams, M.J. & S.J. Hook 1995 Simulated Aster data for geologic studies – IEEE Trans. Geosci. Rem. Sens. 33: 692–699

Adams, J.B. 1974 Visible and near-infrared diffuse reflectance: Spectra of pyroxenes as applied to remote sensing of solid objects in the solar system – J. Geophys. Res. 79: 4829–4836

Adams, J.B. 1975 Interpretation of visible and near-infrared diffuse reflectance spectra of pyroxenes and other rock forming minerals. In: Karr, C. (ed.) Infrared and Raman Spectroscopy of Lunar and Terrestrial Materials. Academic Press, New York: 91–116

Baumgardner, M.F., E.R. Stoner, L.F. Silva & L.L. Biehl 1985 Reflectance properties of soils. In: Brady, N. (ed.) Advances of Agronomy. Academic Press, New York: 1–44

Ben-Dor, E. & F.A. Kruse 1994 The relationship between the size of spatial subsets of GER 63 channel scanner data and the quality of the Internal Average Relative Reflectance (IARR) Atmospheric correction technique – Int. J. Remote Sens. 15: 683–690

Benediktsson, J.A. 1995 Classification and feature extraction from AVIRIS data – IEEE Trans. Geosci. Rem. Sens. 33: 1194–1205

Boardman, J.W., F.A. Kruse & R.O. Green 1995 Mapping target signatures via partial unmixing of AVIRIS data. In: Summaries Fifth Annual JPL Airborne Earth Science Workshop. JPL Publication 95–1, Pasadena: 23–26

Boochs, F., G. Kupfer, K. Dockter & W. Kuhbauch 1990 Shape of the red edge as vitality indicator for plants – Int. J. Remote Sens. 11: 1741–1753

Bowers, T.L. & L.C. Rowan 1996 Remote mineralogic and lithologic mapping of the Ice River Complex, British Columbia, Canada, using AVIRIS data – Photogramm. Eng. Remote Sens. 62: 1379–1385

Burns, R.G. 1970 Mineralogical Application to Crystal Field Theory. Cambridge University Press, Cambridge, 224 pp

Carrere, V. & J.E. Conel 1993 Recovery of atmospheric water vapour total column abundance from imaging spectrometer data around 940 nm – sensitivity analysis and application to Airborne Visible/Infrared Imaging Spectrometer (AVIRIS) data – Remote Sens. Environ. 44: 179–204

Cetin, H. & D.W. Levandowski 1991 Interactive classification and mapping of multi-dimensional remotely sensed data using n-dimensional probability density function (nPDF) – Photogramm. Eng. Remote Sens. 57: 1579–1587

Cetin, H., T.A. Warner. & D.W. Levandowski 1993 Data classification, visualization, and enhancement using n-dimensional probability density functions (nPDF): AVIRIS, TIMS, TM, and Geophysical Applications – Photogramm. Eng. Remote Sens. 59: 1755–1764

Chiu, H.Y. & W. Collins 1978 A spectroradiometer for airborne remote sensing – Photogramm. Eng. Remote Sens. 44: 507–517

Clark, R.N. & T.L. Roush 1984 Reflectance spectroscopy: Quantitative analysis techniques for remote sensing applications – J. Geophys. Res. 89: 6329–6340

Clark, R.N., T.V.V. King, M. Kleijwa, G.A. Swayze & N. Vergo 1990a High spectral resolution reflectance spectroscopy of minerals – J. Geophys. Res. 95: 12653–12680

Clark, R.N., A. Gallagher & G.A. Swayze 1990b Material absorption band depth mapping of imaging spectrometer data using a complete band shape least-squares fit with library reference spectra. In: Green, R.O. (ed.) Proc. Second Airborne Visible/Infrared Imaging Spectrometer (AVIRIS) Workshop. NASA-JPL Publication 90–54, Pasadena: 176–186

Collins, W., S.H. Chang, G. Raines, F. Canney & R. Ashley 1983 Airborne biogeochemical mapping of hidden mineral deposits – Econ. Geol. 78: 737–749

Condit, H.R. 1970 The spectral reflectance of American soils – Photogramm. Eng. Remote Sens. 36: 955–966

Crowley, J.K. & G.A. Swayze 1995 Mapping minerals, amorphous materials, environmental materials, vegetation, water, ice, and other materials: The USGS Tricorder Algorithm. In: Green, R. (ed.) Summaries Fifth Annual JPL Airborne Earth Science Workshop. NASA-JPL Publication 95–1, Pasadena: 39–40

Crowley, J.K., D.W. Brickey & L.C. Rowan 1989 Airborne imaging spectrometer data of the Ruby mountains, Montana: mineral discrimination using relative absorption band-depth images – Remote Sens. Environ. 29: 121–134

Curran, P.J. & J.L. Dungan 1989 Estimation of signal-to-noise: a new procedure applied to AVIRIS data – IEEE Trans. Geosci. Rem. Sens. 27: 620–628

De Jong, S.M. 1998 Imaging spectrometry for monitoring tree damage caused by volcanic activity in the Long Valley Caldera, California – ITC Journal, 1998-1: 1–10

Elvidge, C.D. 1990 Visible and near infrared reflectance characteristics of dry plant material – Int. J. Remote Sens. 11: 1775–1795

Farrand, W.H. & J.C. Harsanyi 1997 Mapping the distribution of mine tailings in the Coeur d'Alene River valley, Idaho, through the use of a Constrained Energy Minimization Technique – Remote Sens. Environ. 59: 64–76

Ferrier, G. & G. Wadge 1996 The application of imaging spectrometry data to mapping alteration zones associated with gold mineralization in southern Spain – Int. J. Remote Sens. 17: 331 – 350

Frouin, R., P.Y. Deschamps & P. Lecomte 1990 Determination from space of atmospheric total water amounts by differential absorption near 940 nm: Theory and airborne verification – J. Appl. Meteorol. 29: 448–460

Gao, B.C. 1993 An operational method for estimating signal to noise ratios from data acquired with imaging spectrometers – Remote Sens. Environ. 43: 23–33

Gao, B.C. & A.F.H. Goetz 1990 Column atmospheric water vapor and vegetation liquid water retrievals from airborne imaging spectrometer data – J. Geophys. Res. 95: 3549–3564

Gao, B.C. & A.F.H. Goetz 1995 Retrieval of equivalent water thickness and information related to biochemical components of vegetation canopies from AVIRIS data – Remote Sens. Environ. 52: 155–162

Goetz, A.F.H. 1991 Imaging spectrometry for studying earth, air, fire and water – EARSel Advances Remote Sens. 1: 3–15

Goetz, A.F.H. 1992 Principles of narrow band spectrometry in the visible and IR: instruments and data analysis. In: Toselli, F. & J. Bodechtel (eds) Imaging Spectroscopy: Fundamentals and Prospective Applications. Kluwer, Dordrecht: 21–32

Goetz, A.H. & M. Herring 1989 The High Resolution Imaging Spectrometer for EOS – IEEE Trans. Geosci. Rem. Sens. 27: 136–144

Goetz, A.F.H. & L.C. Rowan 1981 Geologic remote sensing – Science 211: 781–791

Goetz, A.F.H., L.C. Rowan & M.J. Kingston 1982 Mineral identification from orbit: initial results from the Shuttle Multispectral Infrared Radiometer – Science 218: 1020–1031

Green, A.A. & M.D. Graig 1985 Analysis of aircraft spectrometer data with logarithmic residuals. In: Vane, G. & A.F.H. Goetz (eds) Proc. Airborne Imaging Spectrometer Data Analysis Workshop. NASA-JPL Publication 85–41, Pasadena: 111–119

Green, A.A., M. Berman, P. Switzer & M.D. Graig 1988b A transformation for ordering multispectral data in terms of image quality with implications for noise removal – IEEE Trans. Geosci. Rem. Sens. 26: 65–74

Green, R.O. 1992 Determination of the in-flight spectral and radiometric characteristics of the Airborne Visible/Infrared Imaging Spectrometer (AVIRIS). In: Toselli, F. & J. Bodechtel (eds) Imaging Spectrometry: Fundamentals and Prospective Applications. Kluwer, Dordrecht: 103–123

Green, R.O., G. Vane & J.E. Conel 1988a Determination of in-flight AVIRIS spectral, radiometric, spectral and signal-to-noise characteristics using atmospheric and surface measurements from the vicinity of the rare-earth-bearing carbonatite at Mountain Pass, California. In: Vane, G. (ed.) Proc. Airborne Visible/Infrared Imaging Spectrometer (AVIRIS) Performance Evaluation Workshop. NASA-JPL Publication 88-38, Pasadena: 162–184

Grove, C.I., S.J. Hook & E.D. Paylor II 1992 Laboratory Reflectance Spectra of 160 minerals, 0.4 to 2.5 Micrometers. NASA-JPL Publication 92-2, Pasadena, 300 pp

Hunt, G.R. 1977 Spectral signatures of particulate minerals in the visible and near-infrared – Geophysics 42: 501–513

Hunt, G.R. 1980 Electromagnetic radiation: the communication link in remote sensing. In: Siegal, B. & A. Gillespie (eds) Remote Sensing in Geology. Wiley, New York, 702 pp

Hunt, G.R. & R.C. Evarts 1981 The use of near-infrared spectroscopy to determine the degree of serpentinization of ultramafic rocks – Geophysics 46: 316–321

Hunt, G.R. & J.W. Salisbury 1970 Visible and near-infrared spectra of minerals and rocks, I. Silicate Minerals – Modern Geology 1: 283–300

Hunt, G.R., J.W. Salisbury & C.J. Lenhoff 1973 Visible and near-infrared spectra of minerals and rocks, VII. Acidic Igneous Rocks – Modern Geology 4: 217–224

Ichoku, C. & A. Karnieli 1996 A review of mixture modelling techniques for sub-pixel land cover estimation – Remote Sens. Reviews 13: 161–186

Jia, X. & J.A. Richards 1993 Binary coding of imaging spectrometer data for fast spectral matching and classification – Remote Sens. Environ. 43: 47–53

Kahle, A.B., F.D. Palluconi, S.J. Hook, V.J. Realmuto & G. Bothwell 1991 The Advanced Spaceborne Thermal Emission and Reflectance Radiometer (ASTER) – Int. J. Imag. Syst. Techn. 3: 144–156

Kerekes, J.P. & D.A. Landgrebe 1991 Parameter trade-offs for imaging spectroscopy systems – IEEE Trans. Geosci. Rem. Sens. 29: 57–65

Kruse, F.A. 1988 Use of airborne imaging spectrometer data to map minerals associated with hydrotheramlly altered rocks in the Northern Grapevine Mountains, Nevada, and California – Remote Sens. Environ. 24: 31–51

Kruse, F.A., G.L. Raines & K. Watson 1985 Analytical techniques for extracting geologic information from multichannel airborne spectroradiometer and airborne imaging spectrometer data. In: Proc. Fourth Thematic Conference Remote Sensing Exploration Geology, ERIM, 1–4 April, San Francisco, U.S.A.: 309–324

Kruse, F.A., K.S. Keirein-Young & J.W. Boardman 1990 Mineral mapping at Cuprite, Nevada with a 63-channel imaging spectrometer – Photogramm. Eng. Remote Sens. 56: 83–92

Kruse, F.A., A.B. Lefkoff, J.W. Boardman, K.B. Heidebrecht, A.T. Shapiro, P.J. Barloon & A.F.H. Goetz 1993 The Spectral Image Processing System (SIPS) – interactive visualization and analysis of imaging spectrometer data – Remote Sens. Environ. 44: 145–163

Lee, C. & D.A. Landgrebe 1993 Analyzing high-dimensional multispectral data – IEEE Trans. Geosci. Rem. Sens. 31: 792–800

Lehmann, F., H. Rothfuß & R. Richter 1990 Evaluation of imaging spectrometer data (GER) for the spectral analysis of an old vegetation covered waste deposit. In: Proc. 10th Internat. Geosci. & Remote Sens. Sympos., IGARSS '90, May 20–24, Washington D.C., U.S.A.: 1613–1616

McCauley, J.F., G.G. Schaber, C.S. Breed, M.J. Grolier, C.V. Haynes, B. Issawi & R. Blom 1982 Subsurface valleys and geoarcheology of the Eastern Sahara revealed by shuttle radar – Science 218: 1004–1021

Meyer, P. 1994 A parametric approach for the geocoding of Airborne Visible/Infrared Imaging Spectrometer (AVIRIS) data in rugged terrain – Remote Sens. Environ. 49: 118–130

Nash, D.B. & J.E. Conel 1974 Spectral reflectance systematics for mixtures of powdered hypersthene, labradorite, and ilmenite – J. Geophys. Res. 79: 1615–1621

Okada, K., & A. Iwashita 1992 Hyper-multispectral image analysis based on waveform characteristics of spectral curve – Adv. Space Res. 12: 433–442

Rast, M. 1992 ESA's Activities in the field of imaging spectroscopy. In: Toselli, F. & J. Bodechtel (eds) Imaging Spectroscopy: Fundamentals and Prospective Applications. Kluwer, Dordrecht: 167–191

Rast, M. & J.L. Bézy 1995. The ESA Medium Resolution Imaging Spectrometer (MERIS): requirements to its mission and performance of its system. In: Curran, P.J. & C. Robertson (eds) Proc. RSS'95 'Remote Sensing in Action' 11–14 September 1995, Southampton, U.K.: 125–132

Rast, M., S.J. Hook, C.D. Elvidge & R.E. Alley 1991 An evaluation of techniques for the extraction of mineral absorption features from high spectral resolution remote sensing data – Photogramm. Eng. Remote Sens. 57: 1303–1309

Richter, R. 1996a A spatially adaptive fast atmospheric correction algorithm – Int. J. Remote Sens. 17: 1201–1214

Richter, R. 1996b Atmospheric correction of DAIS hyperspectral data – Comp. Geosci. 22: 785–793

Roberts, D.A., Y. Yamaguchi & R.J.P. Lyon 1985 Calibration of airborne imaging spectrometer data to percent reflectance using field spectral measurements. In: Proc. 19th Internat. Sympos. Remote Sens. Environment, ERIM, 21–25 October, Ann Arbor, U.S.A.: 679–688

Rowan, L.C., C. Anton-Pancheco, D.W. Brickey, M.J. Kingston, A. Payas, N. Vergo & J.K. Crowley 1987 Digital classification of contact metamorphic rocks in Extremadura, Spain using Landsat Thematic Mapper data – Geophysics 52: 885–897

Settle, J.J. & N.A. Drake 1993 Linear mixing and the estimation of ground cover proportions – Int. J. Remote Sens. 14: 1159–1177

Singer, R.B. 1981 Near-infrared spectral reflectance of mineral mixtures: Systematic combinations of pyroxenes, olivine, and iron oxides – J. Geophys. Res. 86: 7967–7982

Staenz, K. 1992 A decade of imaging spectrometry in Canada – Can. J. Remote Sens. 18: 187–197

Van der Meer, F. 1994a Calibration of Airborne Visible/Infrared Imaging Spectrometer data (AVIRIS) to reflectance and mineral mapping in hydrothermal alteration zones: an example from the 'Cuprite Mining District' – Geocarto Int. 9(3): 23–37

Van der Meer, F. 1994b Extraction of mineral absorption features from high-spectral resolution data using non-parametric geostatistical techniques – Int. J. Remote Sens. 15: 2193–2214

Van der Meer, F. 1995 Estimating and simulating the degree of serpentinization of peridotites using hyperspectral remotely sensed imagery – Nonrenewable Resources 4: 84–98

Van der Meer, F. 1996a Performance of the indicator classifier on simulated image data – Int. J. Remote Sens. 17: 621–627

Van der Meer, F. 1996b Metamorphic facies zonation in the Ronda peridotites mapped from GER imaging spectrometer data – Int. J. Remote Sens. 17: 1633–1657

Van der Meer, F. & W. Bakker 1997a CCSM: Cross Correlogram Spectral Matching – Int. J. Remote Sens. 18: 1197–1201

Van der Meer, F. & W. Bakker 1997b Cross Correlogram Spectral Matching (CCSM): application to surface mineralogical mapping using AVIRIS data from Cuprite, Nevada – Remote Sens. Environ. 61: 371–382

Van der Meer, F. & W. Bakker 1998 Validated surface mineralogy from high-spectral resolution remote sensing: a review and a novel approach applied to gold exploration using AVIRIS data – Terra Nova 10: 112–119

Vane, G. & A.F.H. Goetz 1988 Terrestrial imaging spectroscopy – Remote Sens. Environ. 24: 1–29

Vane, G. & A.F.H. Goetz 1993 Terrestrial Imaging Spectrometry: Current Status, Future Trends – Remote Sens. Environ. 44: 117–126

Vane, G., R.O. Green, T.G. Chrien, H.T. Enmark, E.G. Hansen & W.M. Porter 1993 The Airborne Visible/Infrared Imaging Spectrometer (AVIRIS) – Remote Sens. Environ. 44: 127–143

Windeler, D.S. & R.J.P. Lyon 1991 Discriminating dolomitization of marble in the Ludwig Skarn near Yerington, Nevada using high-resolution airborne infrared imagery – Photogramm. Eng. Remote Sens. 57: 1171–1177

Yang, H., J. Zhang, F. van der Meer & S.B. Kroonenberg 1999 Spectral characteristics of wheat associated with hydrocarbon microseepages – Int. J. Remote Sens. 20: 807–813

Zagolski, F. & J.P. Gastellu-Etchegorry 1995 Atmospheric correction of AVIRIS images with a procedure based on the inversion of the 5S model – Int. J. Remote Sens. 16: 3115–3146